

**Fishbone resonance structure in the attosecond transient absorption spectrum of graphene**Fulong Dong  and Jie Liu \**Graduate School, China Academy of Engineering Physics, Beijing 100193, China* (Received 29 September 2022; revised 24 November 2022; accepted 14 December 2022; published 21 December 2022)

We investigate the attosecond transient absorption spectrum (ATAS) of graphene by numerically solving four-band density-matrix equations, which demonstrates apparent “fishbone” resonance structures. To gain insight into these interesting structures, we exploit a simplified model that considers only the electrons of  $\Gamma$  and M points in the Brillouin zone. With the help of this model, we can analytically express the ATAS as the sum of zeroth- and first-order Bessel functions in the variables of the strength and frequency of the infrared pump field as well as the effective mass of electrons at the  $\Gamma$  and M points. Lorentzian and Fano line shapes in the absorption spectrum are addressed. The fishbone structure consists of a periodic V-shaped structure that can be explained by first-order Bessel functions, and its tilt angle is solely determined by the frequency of the pump laser. The periodicity of the V-shaped structure in the fishbone originates from the periodic dependence of the Lorentzian and Fano line shapes of the absorption spectrum on the time delay between the pump and probe lasers. Compared with the numerical results, our analytical theory can qualitatively or even quantitatively predict the zeroth- and first-order fringes in the fishbone structures of the ATAS.

DOI: [10.1103/PhysRevA.106.063107](https://doi.org/10.1103/PhysRevA.106.063107)**I. INTRODUCTION**

Recent progress in laser technology has enabled the production of an isolated pulse with a timescale down to 43 attoseconds [1–3], which allows investigation of electron dynamics on an ultrashort timescale [4]. One promising approach to investigate the subfemtosecond dynamics of electronic systems is attosecond transient absorption spectrum (ATAS) [5–8], which offers an all-optical approach to reveal light-matter interactions with the high temporal resolution of the attosecond pulse and the high-energy resolution characteristic of absorption spectrum. ATAS has been used to study the electron dynamics of atoms and molecules [9–14], in which quantum interference [15], nonresonant AC Stark shift [16], and resonant Autler-Townes splitting [17,18] phenomena have been studied. More recently, attosecond time-resolved technology has been applied to bulk solids [14,19–24] and some two-dimensional (2D) materials [25,26]. For these materials with periodic atomic arrangements, some special subcycle structures emerge in the ATAS [20,25,27–29].

Graphene is a simple but specific 2D material, in which there are only two carbon atoms per unit cell and the atoms are orderly arranged in a periodic hexagonal lattice. The unique electronic structure of graphene [30,31] exhibits a variety of nonlinear optical processes [32–36]. Recently the ATAS in graphene has also been studied [26], where a semiclassical theory is developed to reproduce the ATAS obtained by solving four-band density-matrix equations.

In this work, we investigate the ATAS of graphene with addressing the interesting “fishbone” resonance structure analytically. Our extensive numerical explorations suggest that the 2D four-band model can be simplified to a one-dimensional (1D) four-band model and finally to a two-state

system with a correction of the effective mass term at the  $\Gamma$  and M points. With this maximal simplification, we can approximately express the ATAS as the sum of zeroth- and first-order Bessel functions in the variables of the strength and frequency of the infrared (IR) pump field as well as the effective mass of electrons at the  $\Gamma$  and M points. We find that the V-shaped structure of the fishbone can be explained by first-order Bessel functions. The periodicity of the V-shaped structure in the fishbone originates from the periodic dependence of the Lorentzian or Fano line shape of the absorption spectrum on the time delay between the IR pump and the attosecond x-ray probe lasers. Our analytical theory is compared with the numerical results obtained by directly solving four-band density-matrix equations.

This paper is organized as follows. We describe our calculation methods and numerical results of the ATAS for graphene in Sec. II. Section III shows the analytical formula of the resonance structure of the ATAS. Finally, Sec. IV presents our conclusion. Throughout the paper, atomic units are used if not specified.

**II. DENSITY-MATRIX EQUATIONS AND ATAS**

Graphene is a 2D single layer of carbon atoms arranged in a honeycomb lattice structure [31] as shown in Fig. 1(a), which consists of two sublattices with atoms labeled “A” and “B.” The lattice vectors ( $\mathbf{a}_1 = \frac{d}{2}(3, \sqrt{3})$  and  $\mathbf{a}_2 = \frac{d}{2}(3, -\sqrt{3})$  where  $d = 1.42 \text{ \AA}$  is the carbon-carbon distance) and the nearest-neighbor vectors ( $\delta_i$ ,  $i = 1, 2, 3$ ) are also presented in Fig. 1(a). The first Brillouin zone of graphene is shown in Fig. 1(b), in which  $\mathbf{b}_1 = \frac{2\pi}{3d}(1, \sqrt{3})$  and  $\mathbf{b}_2 = \frac{2\pi}{3d}(1, -\sqrt{3})$  are the reciprocal-lattice vectors and high symmetry points ( $\Gamma$ , M, and K) are marked.

In this work we consider four energy bands of graphene consisting of two core bands ( $g_1$  and  $g_2$ ), which arise from the

\*jliu@gscaep.ac.cn

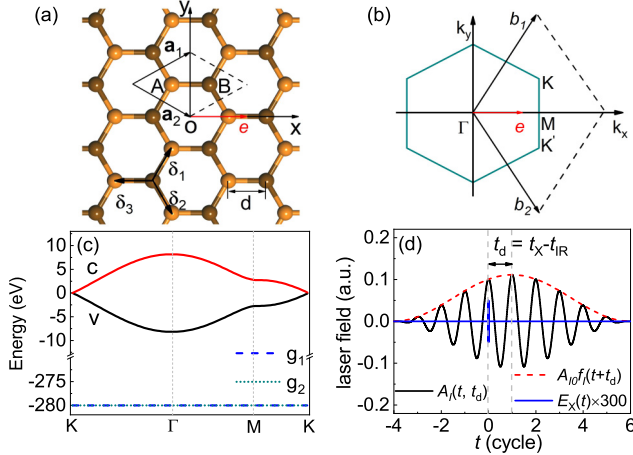


FIG. 1. (a) Hexagonal lattice structure of 2D graphene. Each primitive cell contains two atoms labeled “A” and “B.”  $\mathbf{a}_1$  and  $\mathbf{a}_2$  are the lattice vectors, and  $\delta_i$ ,  $i = 1, 2, 3$ , are the nearest-neighbor vectors.  $\mathbf{e}$  is the unit vector that indicates the polarization direction of the electric field.  $d$  is the carbon-carbon distance. (b) First Brillouin zone of graphene with high-symmetry points  $\Gamma$ , M, and K.  $\mathbf{b}_1$  and  $\mathbf{b}_2$  are the reciprocal-lattice vectors. (c) 2D four-band structure of graphene. (d) Schematic of the time delay between the IR pump laser and x-ray probe pulse.

two  $1s$  orbitals of the two carbon atoms in a unit cell, and the valence ( $v$ ) and conduction ( $c$ ) bands, which arise from the  $\pi$  orbitals orthogonal to the monolayer. The two core bands are degenerate and have a constant energy of  $-280$  eV over the  $\mathbf{k}$  space, as shown in Fig. 1(c).

Utilizing the Bloch states as the basis set, the tight-binding Hamiltonian  $H_0$  arising from the  $\pi$  orbitals of graphene has the form  $H_0 = \begin{pmatrix} 0 & \gamma_0 f(\mathbf{k}) \\ \gamma_0 f^*(\mathbf{k}) & 0 \end{pmatrix}$ , in which electrons can only hop to nearest-neighbor atoms with hopping energy  $\gamma_0 = 0.1$  a.u. and  $f(\mathbf{k}) = e^{i\mathbf{k}_x d} + 2 \cos(\sqrt{3}\mathbf{k}_y d/2) e^{-i\mathbf{k}_x d/2}$ . Diagonalization of the  $H_0$  matrix can yield energy eigenvalues, which describe the dispersion relation of the  $c$  and  $v$  bands  $\varepsilon_c(\mathbf{k}) = -\varepsilon_v(\mathbf{k}) = \gamma_0 |f(\mathbf{k})| = \gamma_0 \sqrt{3 + 2 \cos(\sqrt{3}\mathbf{k}_y d) + 4 \cos(3\mathbf{k}_x d/2) \cos(\sqrt{3}\mathbf{k}_y d/2)}$ .

#### A. Four-band density-matrix equations

We numerically simulate the ATAS of graphene in the length gauge by using the density-matrix equations in which the four energy bands have been included [26]. Within the dipole approximation, these equations read

$$i \frac{\partial}{\partial t} \rho_{mn}(\mathbf{k}, t, t_d) = [\varepsilon_m(\mathbf{k}) - \varepsilon_n(\mathbf{k}) - i\Gamma_{mn}] \rho_{mn}(\mathbf{k}, t, t_d) + i\mathbf{E}_I(t, t_d) \cdot \frac{\partial}{\partial \mathbf{k}} \rho_{mn}(\mathbf{k}, t, t_d) + [\mathbf{E}_I(t, t_d) + \mathbf{E}_X(t)] \cdot [\hat{\mathbf{D}}, \hat{\rho}]_{mn}, \quad (1)$$

where  $m$  and  $n$  represent  $g_1$ ,  $g_2$ ,  $v$ , or  $c$  band, as shown in Fig. 1(c), and  $\Gamma_{mn}$  are the relaxation parameters.

For the 2D four-band structure of graphene in Fig. 1(c), the transition dipole elements associated

with core bands are  $\mathbf{D}_{g_1 g_2}(\mathbf{k}) = \mathbf{D}_{g_1 c}(\mathbf{k}) = \mathbf{D}_{g_2 v}(\mathbf{k}) = 0$ ,  $\mathbf{D}_{g_1 g_1}(\mathbf{k}) = \mathbf{D}_{g_2 g_2}(\mathbf{k}) = 0$ , and  $\mathbf{D}_{g_1 v}(\mathbf{k}) = \mathbf{D}_{g_2 c}(\mathbf{k}) = r_z \mathbf{e}_z$  (see Appendix A for the detailed derivation and discussion). Here  $r_z = \int dz \phi_s^*(z) z \phi_p(z) = 0.041 \text{ \AA}$  [26], in which  $\phi_s(z)$  and  $\phi_p(z)$  are the wave functions of the  $1s$  and  $2p_z$  orbitals along the  $z$  direction. In addition, the transition dipole elements between the  $c$  and  $v$  bands are  $\mathbf{D}_{cv}(\mathbf{k}) = \mathbf{D}_{vc}(\mathbf{k}) = \partial_{\mathbf{k}} \varphi_{\mathbf{k}}/2$  with  $\varphi_{\mathbf{k}} = \text{Arg}[f(\mathbf{k})]$  and  $\mathbf{D}_{cc}(\mathbf{k}) = \mathbf{D}_{vv}(\mathbf{k}) = 0$  [26,37,38].

$\mathbf{E}_X(t) = E_X f_X(t) \cos(\omega_X t) \mathbf{e}_z$  is the electric field of the x-ray pulse, in which  $f_X(t) = e^{-(4\ln 2)(t/\tau_X)^2}$  has a full width at half maximum of  $\tau_X = 80$  attoseconds and the amplitude  $E_X$  corresponds to the intensity of  $1 \times 10^9 \text{ W/cm}^2$ . The frequency of the x-ray pulse is  $\omega_X = 280 \text{ eV}$ , which is equal to the energy gap between the Fermi surface and the core bands.  $\mathbf{e}_z$  is the unit vector perpendicular to the graphene monolayer.

$\mathbf{A}_I(t, t_d) = A_{I0} f_I(t + t_d) \cos(\omega_I t + \omega_I t_d) \mathbf{e}$  is the vector potential of the IR laser field.  $f_I(t) = \cos^2(\omega_I t/2n)$  is an envelope with  $n = 10$  and the amplitude of  $A_{I0}$  corresponds to a laser intensity of  $1 \times 10^{11} \text{ W/cm}^2$ .  $\omega_I$  is the frequency of the IR laser field, corresponding to the wavelength of  $\lambda = 3000 \text{ nm}$ .  $T = 2\pi/\omega_I$  is the period of the IR laser field.  $\mathbf{e}$  is the unit vector along the  $\Gamma - \text{M}$  direction of graphene. The electric field of the IR laser is calculated by  $\mathbf{E}_I(t, t_d) = -\partial \mathbf{A}_I(t, t_d)/\partial t$ . As shown in Fig. 1(d),  $t_d = t_X - t_{IR}$  is the time delay, where  $t_X = 0$  and  $t_{IR}$  are the maximums of the x-ray pulse and IR laser field envelopes, respectively. When  $t_d = 0$ , the maximum values of both pulses overlap. Note that the ATAS results only depend on the relative time delay  $t_d$  rather than the absolute time  $t_X$  or  $t_{IR}$ . Therefore, one can either choose  $t_X$  or  $t_{IR}$  as time origin. In the present work, to simplify the analytic deductions of ATAS appearing in the following sections, we prefer to set  $t_X = 0$ .

The computational complexity introduced by the gradients in Eq. (1) can be removed by transforming the crystal momentum  $\mathbf{k}$  into a frame moving one  $\mathbf{k}_t = \mathbf{k} + \mathbf{A}_I(t, t_d)$  [39]. Under this transformation, the partial differential equation (1) reduce to ordinary differential equation,

$$i \frac{d}{dt} \rho_{mn}(\mathbf{k}_t, t, t_d) = [\varepsilon_m(\mathbf{k}_t) - \varepsilon_n(\mathbf{k}_t) - i\Gamma_{mn}] \rho_{mn}(\mathbf{k}_t, t, t_d) + [\mathbf{E}_I(t, t_d) + \mathbf{E}_X(t)] \cdot \sum_l [\mathbf{D}_{ml}(\mathbf{k}_t) \times \rho_{ln}(\mathbf{k}_t, t, t_d) - \rho_{ml}(\mathbf{k}_t, t, t_d) \mathbf{D}_{ln}(\mathbf{k}_t)], \quad (2)$$

which can be readily numerically solved by the standard fourth-order Runge-Kutta algorithm.

At  $t = -\infty$ , electrons populate the two core bands and the valence band; thus,  $\rho_{g_1 g_1}(\mathbf{k}_t, t = -\infty, t_d) = \rho_{g_2 g_2}(\mathbf{k}_t, t = -\infty, t_d) = \rho_{vv}(\mathbf{k}_t, t = -\infty, t_d) = 1$ , and the other terms of the density matrix elements are zero. The core-hole lifetime is about 6.1 fs [26] and the corresponding relaxation parameters  $\Gamma_{g_1 v} = \Gamma_{g_1 c} = \Gamma_{g_2 v} = \Gamma_{g_2 c} = \Gamma_{cv} = 0.004 \text{ a.u.} \equiv \Gamma_0$ . Because the population relaxation is much slower than the decoherence time, we set the population relaxation parameters  $\Gamma_{g_1 g_1} = \Gamma_{g_2 g_2} = \Gamma_{cc} = \Gamma_{vv} = 0$ . On the other hand,  $\Gamma_{g_1 g_2}$  is set to be zero because there is no transition between  $g_1$  and  $g_2$  bands.

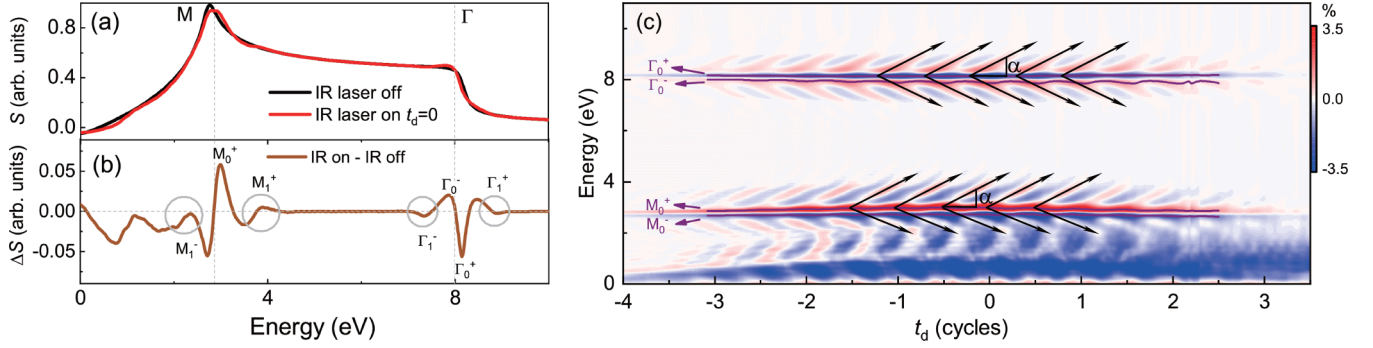


FIG. 2. (a) X-ray response functions of graphene without and with IR laser field of  $t_d = 0$ , which are calculated by Eq. (3) based on the density-matrix equations (2). (b) Corresponding ATAS at  $t_d = 0$  evaluated by Eq. (5). In (b),  $M_0^-$ ,  $M_0^+$  and  $\Gamma_0^-$ ,  $\Gamma_0^+$  indicate the zeroth-order resonance peaks around M and  $\Gamma$  points, respectively, and  $M_1^-$ ,  $M_1^+$ ,  $\Gamma_1^-$ , and  $\Gamma_1^+$  labeled by gray rings are the first-order resonance structures. (c) ATAS as a function of the time delay in units of IR laser cycles. In (c) the black solid arrows indicate the V-shaped structure, and  $\alpha$  is the tilt angle. The purple curves mark the zeroth-order resonance peaks that vary slowly with time delay  $t_d$ . In contrast, the first-order resonance structures periodically change with it.

The x-ray response function for time delay  $t_d$  is calculated by [6]

$$S(\omega, t_d) = 2 \text{Im}[\tilde{\mu}(\omega, t_d)\tilde{E}_X^*(\omega)], \quad (3)$$

where  $\tilde{E}_X(\omega)$  is the Fourier transform of  $E_X(t)$ , and  $\tilde{E}_X^*(\omega)$  represents the complex conjugate of  $\tilde{E}_X(\omega)$ .  $\tilde{\mu}(\omega, t_d)$  is the Fourier transform of  $\mu(t, t_d)$ , which is calculated by

$$\mu(t, t_d) = \sum_{\mathbf{k}} \sum_{i,g} [r_z \rho_{ig}(\mathbf{k}_t, t, t_d) + \text{c.c.}], \quad (4)$$

where  $g$  represents the  $g_1$  or  $g_2$  band and  $i$  represents the  $v$  or  $c$  band.

The ATAS can then be calculated according to

$$\Delta S(\omega, t_d) = S(\omega, t_d) - S^X(\omega), \quad (5)$$

where  $S^X(\omega)$  is the x-ray response function without IR laser field.

### B. ATAS from numerically solving density-matrix equations

By numerically solving the above four-band density-matrix equations, we calculate the ATAS in the length gauge. Figure 2(a) shows the x-ray response functions of graphene without and with an IR laser field of  $t_d = 0$ , which are calculated by Eq. (3) based on the density-matrix equations (2). The corresponding ATAS at  $t_d = 0$  evaluated by Eq. (5) is presented in Fig. 2(b). Figure 2(c) shows the ATAS as a function of the time delay in units of IR laser optical cycles. In the absorption spectrum in Fig. 2(b), we observe interesting zeroth-order resonant peaks  $M_0^-$  and  $M_0^+$  (or  $\Gamma_0^-$  and  $\Gamma_0^+$ ) around M (or  $\Gamma$ ) point, and they vary slowly with time delay  $t_d$  as marked by the purple curves in Fig. 2(c). In contrast, the first-order resonant structures  $M_1^-$  and  $M_1^+$ ,  $\Gamma_1^-$  and  $\Gamma_1^+$  labeled by gray rings in Fig. 2(b) periodically vary with time delay  $t_d$ , as shown in Fig. 2(c). In Fig. 2(c) apparent fishbone structures consisting of the zeroth- and first-order resonant structures around the M point (near 2.72 eV) and  $\Gamma$  point (approximately 8.16 eV) can be observed. The black solid arrows indicate the V-shaped structure (corresponding to local maximums) with a tilt angle of  $\alpha$  in the fishbone structure, which has a period that is  $T/2$ .

Our calculated ATAS shown in Fig. 2(c) is analogous to that of Ref. [26], in which the pulse duration of the IR laser is three optical cycles. In contrast, the energy region of the ATAS in Fig. 2 is from 0 to 11 eV to highlight the fishbone structure. Similar structure has also been observed in an *ab initio* simulation of the ATAS of monolayer hexagonal boron nitride in [25]. The periodicity of the V-shaped structure was found to emerge in other materials, such as diamond and GaAs [20,21], which was attributed to the dynamical Franz-Keldysh effect related to the intraband motion of electrons. Despite these experiments, simulations and theoretical investigations, an explicit mechanism of the fishbone resonance structure in an analytical form is still lacking.

As a comparison, still utilizing the Bloch states as the basis set, we perform additional calculations of ATAS in the velocity gauge. We find that the ATAS near the M point are qualitatively consistent, but, however, an apparent discrepancy exists near the  $\Gamma$  point. In principle, the ATAS results should be gauge-independent. The difference is due to the four-band approximation. To obtain more accurate ATAS near the  $\Gamma$  point, one should consider more conduction bands in the density-matrix equations in the velocity gauge [40,41]. The density-matrix equations in the length gauge describe the electron dynamics implicitly using time-dependent Houston states, which are best thought of as an adiabatic basis [42]. It is applicable to describe the dynamics around M and  $\Gamma$ , while might not be applicable to the K point due to the degeneracy of the energy bands. More interestingly, the Houston states basis set might improve the velocity gauge results. When the Houston states are utilized as the basis set, we find the ATAS of the both gauges are consistent to that shown in Fig. 2(c).

## III. ANALYTICAL INVESTIGATION OF FISHBONE RESONANCE STRUCTURE IN THE ATAS

### A. Simplified model

We first study the influence of intraband and interband transitions on the ATAS. In the 2D four-band model in Fig. 1(c), we block the interband transition between the valence and conduction bands, as shown in Fig. 3(a). The corresponding ATAS is presented in Fig. 3(b). By comparing Fig. 3(b) and

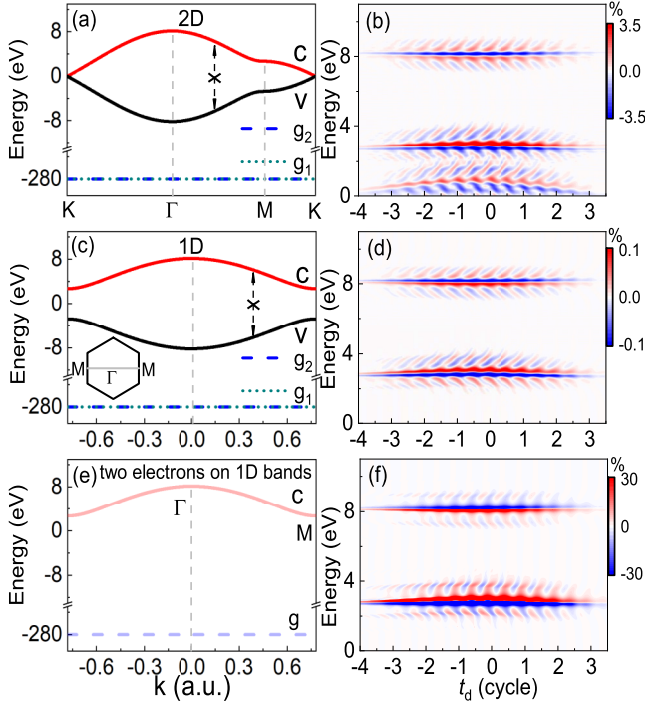


FIG. 3. (a) Schematic of the 2D four-band model in which the transition between the valence and conduction bands has been artificially blocked. (b) ATAS as a function of the time delay in units of IR laser optical cycles, which is calculated using density-matrix equations (2) based on the model in (a). (c) 1D four-band model obtained by taking a section along the  $\Gamma$ -M direction of the 2D energy bands in (a), as presented by the gray line of the inset, where the transition between valence and conduction bands has also been blocked. (d) ATAS corresponding to the model in (c). (e) Simplified model which includes two electrons. The lattice momenta of the electrons are  $\mathbf{k} = 0$  ( $\Gamma$  point) and  $\mathbf{k} \approx 0.78$  a.u. (M point). (f) ATAS based on the simplified model in (e).

Fig. 2(c), one can find that the interband transition has a significant effect on the ATAS near the K point; however, it plays a small role in the spectrum at the  $\Gamma$  and M points. The underlying mechanism is that for the band model in Fig. 1(c), the electrons near the K point can be easily excited from the valence band to the conduction band by the IR laser. This process blocks the transition of electrons from the  $g_2$  band to the  $c$  band under the x-ray pulse excitation and therefore results in an absorption decrease of the  $c$  band, forming the “blue band” near the K point in Fig. 2(c). At the M and  $\Gamma$  points, however, the wider energy gaps block interband transition process caused by the IR laser, and the generation mechanism of the ATAS arises from the intraband dynamics of electrons. In the following work, we mainly investigate the mechanism of the fishbone structure near M and  $\Gamma$  points.

We further simplify our 2D model in Fig. 3(a) to the 1D model in Fig. 3(c) by taking a section along the  $\Gamma - M$  direction of the 2D band structure. The dispersion relations of the 1D bands are  $\epsilon_c(\mathbf{k}) = -\epsilon_v(\mathbf{k}) = \epsilon_c(\mathbf{k} = \mathbf{k}_x, \mathbf{k}_y = 0) = \gamma_0 \sqrt{5 + 4 \cos(3\mathbf{k}d/2)}$  and  $\epsilon_g = \epsilon_{g1}(\mathbf{k}) = \epsilon_{g2}(\mathbf{k}) = -280$  eV. Based on this model, the corresponding ATAS is presented in Fig. 3(d). One can find that the ATAS near the K point disappears, while the fishbone structures around the M and  $\Gamma$

points are well consistent with those in Fig. 3(b). Therefore, we can exploit the 1D model in Fig. 3(c) to study the fishbone structure.

Furthermore, in the band model in Fig. 3(c), the electrons in the  $g_1$  and  $v$  bands cannot jump to the  $g_2$  or  $c$  bands because  $\mathbf{D}_{g_1c}(\mathbf{k}) = \mathbf{D}_{vc}(\mathbf{k}) = \mathbf{D}_{g_1g_2}(\mathbf{k}) = \mathbf{D}_{vg_2}(\mathbf{k}) = 0$ . Additionally, although  $\mathbf{D}_{g_1v}(\mathbf{k}) \neq 0$ , the transition between the  $g_1$  and  $v$  bands is forbidden because  $\rho_{g_1g_1}(\mathbf{k}_t, t, t_d) = \rho_{vv}(\mathbf{k}_t, t, t_d) = 1$ . Therefore, the 1D four-band model in Fig. 3(c) is equivalent to the 1D two-band structure in Fig. 3(e) consisting of  $g \equiv g_2$  and  $c$  bands. We propose the simplified model shown in Fig. 3(e), which includes two electrons with lattice momenta of  $\mathbf{k} = 0$  ( $\Gamma$  point) and  $\mathbf{k} \approx 0.78$  a.u. (M point), and the corresponding ATAS is shown in Fig. 3(f). The fishbone structures of ATAS in Fig. 3(f) are qualitatively consistent with those of Fig. 3(d). In the following, based on this simplified model in Fig. 3(e), we develop an analytical theory to investigate the underlying mechanism of the fishbone structure.

### B. Analytic deduction of ATAS $\Delta S(\omega, t_d)$

Based on the simplified model in Fig. 3(e), we deduce an analytical formula of the ATAS. Because the x-ray pulse is relatively short and weak, it can be approximated to a  $\delta$  function  $E_X(t) = A_X \delta(t)$ . The electrons can be instantaneously excited from the  $g$  band to the  $c$  band by the x-ray pulse at the moment of  $t = 0$ . According to perturbation theory and Eq. (2), the density matrix elements change from  $\rho_{gg}(\mathbf{k}_t, t < 0^-, t_d) = 1$ ,  $\rho_{cc}(\mathbf{k}_t, t < 0^-, t_d) = 0$ , and  $\rho_{cg}(\mathbf{k}_t, t < 0^-, t_d) = 0$  to  $\rho_{gg}(\mathbf{k}_t, t = 0^+, t_d) \approx 1$ ,  $\rho_{cc}(\mathbf{k}_t, t = 0^+, t_d) \approx 0$ , and  $\rho_{cg}(\mathbf{k}_t, t = 0^+, t_d) \approx -iA_X r_z$ . Next, the time-dependent evolution of density matrix elements is dominated only by the IR laser, and one can obtain  $\rho_{cg}(\mathbf{k}_t, t > 0^+, t_d) = -iA_X r_z e^{-i \int_0^t \{\epsilon_c[\mathbf{k} + A_I(t', t_d)] - \epsilon_g\} dt'} e^{-\Gamma_0 t}$ . According to Eq. (4), when  $t < 0^-$ , the time-dependent dipole is  $\mu_{\mathbf{k}}(t, t_d) = 0$ , and when  $t > 0^+$ , it is  $\mu_{\mathbf{k}}(t, t_d) = -2A_X r_z^2 \sin[\int_0^t \{\epsilon_c[\mathbf{k} + A_I(t', t_d)] - \epsilon_g\} dt'] e^{-\Gamma_0 t}$ . Here relaxation parameter  $\Gamma_0 = 0.004$  a.u. is the same as that used in the numerical calculation.

According to Eqs. (3) and (4), the response function is calculated by  $S(\omega, t_d) = \sum_{\mathbf{k}} S_{\mathbf{k}}(\omega, t_d)$  and  $S_{\mathbf{k}}(\omega, t_d) = 2 \text{Im}[\tilde{\mu}_{\mathbf{k}}(\omega, t_d) \tilde{E}_X^*(\omega)] \propto \text{Im}[\tilde{\mu}_{\mathbf{k}}(\omega, t_d)] = \text{Im}[\int_0^\infty \mu_{\mathbf{k}}^X(t) e^{-i\omega t} dt]$ . When the IR laser is off, the response function is  $S_{\mathbf{k}}^X(\omega) \propto \frac{\Gamma_0}{\Gamma_0^2 + [\omega - \epsilon_c(\mathbf{k})]^2} \equiv L[\omega, \epsilon_c(\mathbf{k})]$ , in which  $\mathbf{k} = \mathbf{k}_\Gamma = 0$  or  $\mathbf{k} = \mathbf{k}_M \approx 0.78$ .  $L(\omega, x) = \frac{\Gamma_0}{\Gamma_0^2 + (\omega - x)^2}$  is the Lorentzian line shape centered at  $x$ . (See Appendix B for the detailed derivation. Note that the response function spectra have been shifted by  $\epsilon_g$  in the energy domain.)

When the IR laser is turned on, the response function of the electron at the  $\Gamma$  or M point can be evaluated by  $S_{\mathbf{k}}(\omega, t_d)$ . The analytical expression of the ATAS in general takes following form:

$$\begin{aligned} \Delta S_{\mathbf{k}}(\omega, t_d) &= S_{\mathbf{k}}(\omega, t_d) - S_{\mathbf{k}}^X(\omega) \\ &= \Delta S_{\mathbf{k}}^0(\omega, t_d) + \Delta S_{\mathbf{k}}^1(\omega, t_d), \end{aligned} \quad (6)$$

where  $\Delta S_{\mathbf{k}}^0(\omega, t_d)$  and  $\Delta S_{\mathbf{k}}^1(\omega, t_d)$  are the zeroth- and first-order resonance structures, respectively. We can obtain

$$\Delta S_{\mathbf{k}}^0(\omega, t_d) \propto J_0[b_{\mathbf{k}}(t_d)] L[\omega, \epsilon_s(\mathbf{k}, t_d)] - L[\omega, \epsilon_c(\mathbf{k})] \quad (7)$$

and

$$\begin{aligned} \Delta S_{\mathbf{k}}^1(\omega, t_d) \propto & J_1[b_{\mathbf{k}}(t_d)]L[\omega, \epsilon_s(\mathbf{k}, t_d) + 2\omega_I] \cos(2\omega_I t_d) \\ & + J_1[b_{\mathbf{k}}(t_d)]F[\omega, \epsilon_s(\mathbf{k}, t_d) + 2\omega_I] \sin(2\omega_I t_d) \\ & - J_1[b_{\mathbf{k}}(t_d)]L[\omega, \epsilon_s(\mathbf{k}, t_d) - 2\omega_I] \cos(2\omega_I t_d) \\ & + J_1[b_{\mathbf{k}}(t_d)]F[\omega, \epsilon_s(\mathbf{k}, t_d) - 2\omega_I] \sin(2\omega_I t_d), \end{aligned} \quad (8)$$

where  $F(\omega, x) = \frac{\omega-x}{\Gamma_0^2+(\omega-x)^2}$  is the Fano line shape with  $q$  parameter of 1 centered at  $x$  [43,44]. Here we define  $\epsilon_s(\mathbf{k}, t_d) = \epsilon_c(\mathbf{k}) + A_{I0}^2 f_I^2(t_d)/(4m_{\mathbf{k}}^*)$  and  $b_{\mathbf{k}}(t_d) = A_{I0}^2 f_I^2(t_d)/(8\omega_I m_{\mathbf{k}}^*)$ , where  $m_{\mathbf{k}}^* = 1/\nabla_{\mathbf{k}}^2 \epsilon_c(\mathbf{k})$  is the effective mass.  $J_n(x)$  is the  $n$ th-order Bessel function, and on the right side of Eqs. (7) and (8), the prefactors have been adjusted to be 1.

### C. Resonance peaks in the ATAS

When the IR laser is off, the response function  $S_{\mathbf{k}}^X(\omega) = L[\omega, \epsilon_c(\mathbf{k})]$  (black line) is shown in Fig. 4(a), which presents two Lorentzian line shapes whose peaks are located at  $\epsilon_c(\mathbf{k}_M) \approx 2.72$  eV and  $\epsilon_c(\mathbf{k}_\Gamma) \approx 8.16$  eV.

When the IR laser of  $t_d = 0$  is turned on, the response function (red line in Fig. 4(a)) is  $S_{\mathbf{k}}(\omega, t_d = 0) \propto J_0(b_{0\mathbf{k}})L[\omega, \epsilon_{0s}(\mathbf{k})] + J_1(b_{0\mathbf{k}})L[\omega, \epsilon_{0s}(\mathbf{k}) + 2\omega_I] - J_1(b_{0\mathbf{k}})L[\omega, \epsilon_{0s}(\mathbf{k}) - 2\omega_I]$ , where  $\epsilon_{0s}(\mathbf{k}) = \epsilon_s(\mathbf{k}, t_d = 0) = \epsilon_c(\mathbf{k}) + A_{I0}^2/(4m_{\mathbf{k}}^*)$  and  $b_{0\mathbf{k}} = b_{\mathbf{k}}(t_d = 0) = A_{I0}^2/(8\omega_I m_{\mathbf{k}}^*)$ . Comparing with  $S_{\mathbf{k}}^X(\omega)$ , the zeroth-order resonance peaks associated with  $J_0(b_{0\mathbf{k}})$  term are shifted by  $A_{I0}^2/(4m_{\mathbf{k}}^*)$ . For the electron of the M point (or the  $\Gamma$  point) whose effective mass  $m_{\mathbf{k}_M}^*$  (or  $m_{\mathbf{k}_\Gamma}^*$ ) is 0.3 a.u. (or  $-0.9$  a.u.), the energy shift  $A_{I0}^2/(4m_{\mathbf{k}_M}^*)$  [or  $A_{I0}^2/(4m_{\mathbf{k}_\Gamma}^*)$ ] is equal to 0.27 eV (or  $-0.09$  eV). In addition, when IR laser of  $t_d = 0$  is on, for each electron with lattice momentum  $\mathbf{k}_M$  or  $\mathbf{k}_\Gamma$ , two additional first-order resonance structures associated with  $J_1(b_{0\mathbf{k}})$  terms appear, which exhibit Lorentzian line shape. The energy intervals between the zeroth-order resonance peak and two first-order resonance structures are  $2\omega_I$ , as shown in Fig. 4(a).

In Fig. 4(a) we also show the response function  $S_{\mathbf{k}}(\omega, t_d = -3T/8) \propto J_0(b_{1\mathbf{k}})L[\omega, \epsilon_{1s}(\mathbf{k})] + J_1(b_{1\mathbf{k}})F[\omega, \epsilon_{1s}(\mathbf{k}) + 2\omega_I] + J_1(b_{1\mathbf{k}})F[\omega, \epsilon_{1s}(\mathbf{k}) - 2\omega_I]$ , where  $\epsilon_{1s}(\mathbf{k}) = \epsilon_s(\mathbf{k}, t_d = -3T/8) \approx \epsilon_{0s}(\mathbf{k})$  and  $b_{1\mathbf{k}} = b_{\mathbf{k}}(t_d = -3T/8) \approx b_{0\mathbf{k}}$  for both M and  $\Gamma$  points. In contrast to  $S_{\mathbf{k}}(\omega, t_d = 0)$ , the first-order resonance structures of response function  $S_{\mathbf{k}}(\omega, t_d = -3T/8)$  exhibit the Fano line shape.

Figure 4(b) shows analytical ATAS  $\Delta S_{\mathbf{k}}(\omega, t_d = 0)$  and  $\Delta S_{\mathbf{k}}(\omega, t_d = -3T/8)$  calculated by Eq. (6). One can find two zeroth-order peaks  $M_0^-$  and  $M_0^+$  (or  $\Gamma_0^-$  and  $\Gamma_0^+$ ) corresponding to  $\Delta S_{\mathbf{k}}^0(\omega, t_d)$ , as well as two first-order resonance structures  $M_1^-$  and  $M_1^+$  (or  $\Gamma_1^-$  and  $\Gamma_1^+$ ) labeled by gray rings corresponding to  $\Delta S_{\mathbf{k}}^1(\omega, t_d)$  around the M (or  $\Gamma$ ) point.

In Fig. 4(c), we show numerical ATAS for time delays  $t_d = 0$  and  $t_d = -3T/8$ , which are extracted from Fig. 2(c). Comparing the results in Fig. 4(b) and Fig. 4(c), one can obtain that the zeroth- and first-order resonance structures are qualitatively consistent. Quantitatively, there are some deviations between the analytical and numerical results, especially for the first-order resonance structures, which arise from the fact that our analytical results are based on the simplified

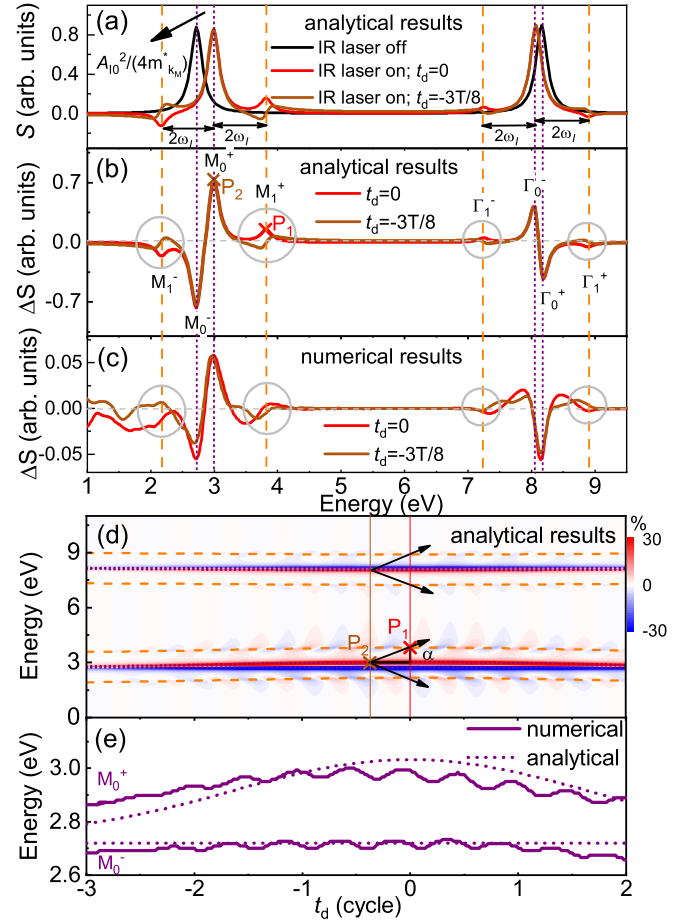


FIG. 4. (a) The analytical response functions  $S_{\mathbf{k}}^X(\omega)$ ,  $S_{\mathbf{k}}(\omega, t_d = 0)$ , and  $S_{\mathbf{k}}(\omega, t_d = -3T/8)$ . (b) Corresponding absorption spectra  $\Delta S_{\mathbf{k}}(\omega, t_d = 0)$  and  $\Delta S_{\mathbf{k}}(\omega, t_d = -3T/8)$ . (c) The numerical ATAS for time delays  $t_d = 0$  and  $t_d = -3T/8$ , which are extracted from Fig. 2(c). In (a), (b), and (c), the vertical purple dotted lines mark the zeroth-order resonance peaks  $M_0^-$ ,  $M_0^+$ ,  $\Gamma_0^-$ , and  $\Gamma_0^+$  that correspond to  $\Delta S_{\mathbf{k}}^0(\omega, t_d)$ , and the vertical orange dashed lines are the centers of first-order resonance structures  $M_1^-$ ,  $M_1^+$ ,  $\Gamma_1^-$ , and  $\Gamma_1^+$  labeled by gray rings, corresponding to  $\Delta S_{\mathbf{k}}^1(\omega, t_d)$ . (d) The analytical ATAS  $\Delta S_{\mathbf{k}}(\omega, t_d)$  calculated by Eq. (6). In (d), the black arrows indicate the V-shaped structure, whose tilt angle is defined as  $\alpha$ . Around the M and  $\Gamma$  points, the horizontal purple dotted lines are  $\epsilon_c(\mathbf{k})$  and  $\epsilon_s(\mathbf{k}, t_d)$ , and the orange dashed lines correspond to  $\epsilon_s(\mathbf{k}, t_d) \pm 2\omega_I$ . In (b) and (d), “ $P_1$ ” and “ $P_2$ ” points labeled by the crosses are local maximum values. In (e), the purple solid curves reproduce  $M_0^-$  and  $M_0^+$  in Fig. 2(c), and the dotted lines are the corresponding analytical results  $\epsilon_c(\mathbf{k}_M)$  and  $\epsilon_s(\mathbf{k}_M, t_d)$ .

model that considers only the electrons of  $\Gamma$  and M points in the Brillouin zone.

### D. V-shaped structure in the ATAS

The analytical ATAS as a function of the time delay, which are calculated by Eq. (6), are shown in Fig. 4(d). The black arrows indicate the V-shaped structure that corresponds to local maximum ATAS amplitudes. According to  $\Delta S_{\mathbf{k}}^0(\omega, t_d)$  of Eq. (7), one can obtain that the zeroth-order resonance peaks vary slowly with time delay  $t_d$ , as shown in Fig. 4(d). In contrast,  $\Delta S_{\mathbf{k}}^1(\omega, t_d)$  of Eq. (8) implies that as the time delay

continuously varies, the first-order resonance structures periodically present Lorentzian or Fano line shapes, forming the V-shaped structure in the ATAS. Corresponding to  $\cos(2\omega_I t_d)$  and  $\sin(2\omega_I t_d)$ , the period of the V-shaped structure is  $T/2$ , as shown in Figs. 4(d) and 2(c). The zeroth- and first-order resonance structures make up the fishbone structure in the ATAS.

We define the tilt angle  $\alpha$  of the V-shaped structure in Fig. 4(d). The horizontal purple dotted lines  $[\epsilon_c(\mathbf{k}), \epsilon_s(\mathbf{k}, t_d)]$  and orange dashed lines  $[\epsilon_s(\mathbf{k}, t_d) \pm 2\omega_I]$  in Fig. 4(d) indicate the centres of the zeroth- and first-order resonance structures. The two vertical solid lines mark the time delays  $t_d = 0$  and  $t_d = -3T/8$ , and corresponding ATAS have been shown in Fig. 4(b). As shown in Figs. 4(d) and 4(b), the  $P_1$  points are local maximal values, which satisfy both  $\frac{\partial}{\partial \omega} \Delta S(\omega, t_d)|_{t_d=0} = 0$  and  $\frac{\partial}{\partial t_d} \Delta S(\omega, t_d)|_{\omega=\epsilon_s(\mathbf{k}_M, t_d)+2\omega_I} = 0$ . The  $P_2$  points satisfy  $\frac{\partial}{\partial \omega} \Delta S(\omega, t_d)|_{t_d=-3T/8} = 0$  and are located at the zeroth-order peak  $M_0^+$ , as shown in Fig. 4(b). The energy and time intervals between points  $P_1$  and  $P_2$  are  $2\omega_I$  and  $3T/8$ , respectively. Therefore, in Fig. 4(d), the tilt angle  $\alpha$  of the V-shaped structure is defined by  $\tan(\alpha) \approx \frac{2\omega_I}{3T/8} = \frac{8\omega_I^2}{3\pi}$ . This implies that the tilt angle of the V-shaped structure increases with the IR laser frequency.

In Fig. 4(e), the two purple solid curves  $M_0^-$  and  $M_0^+$  reproduce the zeroth-order resonance peaks of the fishbone structure near the M point in Fig. 2(c). The two purple dotted lines are the analytical results  $\epsilon_c(\mathbf{k}_M)$  and  $\epsilon_s(\mathbf{k}_M, t_d)$ , corresponding to  $M_0^-$  and  $M_0^+$ , respectively. One can obtain that for different time delays, our analytical theory can qualitatively predict the energy shifts of the zeroth-order fringes of the fishbone structure in the ATAS.

#### IV. CONCLUSION

In summary, we investigate the ATAS of graphene by numerically solving four-band density-matrix equations in the length gauge, which shows apparent fishbone resonance structures. To gain insight into these interesting structures, we develop a simplified model that only considers the electrons of the  $\Gamma$  and M points. With the help of this model, we can obtain an analytical expression of the ATAS that consists of the zeroth- and first-order resonance structures associated with Bessel functions. Our theory predicts that the zeroth-order fringe of the fishbone structure slowly varies with the time delay, while the first-order fringes alternately change between the Lorentzian line shape and Fano line shape at twice the IR laser frequency, leading to the fishbone resonance structure.

Our analytical derivation might be extended to other materials that cannot be described by the same four-band model as that of graphene. It requires only that the electron is injected at a momentum with zero velocity, which will happen generally due to the larger density of states. Therefore, some findings of this paper might be applicable to some other 2D materials or even bulk solids, such as GaAs in Ref. [45]. We hope that our theory will stimulate experiments in the fields.

#### ACKNOWLEDGMENTS

This work is supported by NSAF (Grant No. U1930403). We acknowledge valuable discussions with Prof. Difa Ye.

#### APPENDIX A: TRANSITION DIPOLE ELEMENTS ASSOCIATED WITH CORE BANDS

Graphene is a 2D single layer of carbon atoms arranged in a honeycomb lattice, as shown in Fig. 1(a). The outermost four electrons of all carbon atoms are  $sp^2$  hybridized, and one electron per carbon atom remains in the  $2p_z$  orbital, which extends out of the plane of the chain [31]. The Bloch states formed by the  $2p_z$  orbital sitting on the sublattices A and B can be used as normalized basis set:  $\varphi_{Ap}(\mathbf{k}, \mathbf{r}) = \frac{1}{\sqrt{N}} \sum_j e^{i\mathbf{k}\mathbf{R}_j^A} \phi_p(\mathbf{r} - \mathbf{R}_j^A)$ ,  $\varphi_{Bp}(\mathbf{k}, \mathbf{r}) = \frac{1}{\sqrt{N}} \sum_j e^{i\mathbf{k}\mathbf{R}_j^B} \phi_p(\mathbf{r} - \mathbf{R}_j^B)$ . Here  $j$  is the index of the primitive cell, and  $N$  is the total number of primitive cells.  $\mathbf{R}_j^A$  and  $\mathbf{R}_j^B$  are the position vectors of A and B atoms in the  $j$ th primitive cell.  $\phi_p(\mathbf{r})$  is the wave function of the  $2p_z$  orbital in graphene. The diagonalization of  $H_0$  (i.e., here  $\hat{H}_0$  is a field-free Hamiltonian) matrix can yield the energy eigenvalues which describe the dispersion relation of the  $c$  and  $v$  bands:  $\epsilon_c(\mathbf{k}) = -\epsilon_v(\mathbf{k}) = \gamma_0 |f(\mathbf{k})|$ , and the corresponding eigenvectors are

$$\psi_{v(c)}^{\mathbf{k}}(\mathbf{r}) = c_{A,v(c)} \varphi_{Ap}(\mathbf{k}, \mathbf{r}) + c_{B,v(c)} \varphi_{Bp}(\mathbf{k}, \mathbf{r}), \quad (\text{A1})$$

where  $c_{A,v} = c_{A,c} = \frac{\sqrt{2}}{2} e^{-i\varphi_{\mathbf{k}}/2}$ ,  $c_{B,v} = -c_{B,c} = -\frac{\sqrt{2}}{2} e^{i\varphi_{\mathbf{k}}/2}$ , with  $\varphi_{\mathbf{k}} = \text{Arg}[f(\mathbf{k})]$ .

For the core bands, similarly we have the wave functions of  $g_1$  and  $g_2$  bands are

$$\psi_{g_1(g_2)}^{\mathbf{k}}(\mathbf{r}) = c_{A,g_1(g_2)} \varphi_{As}(\mathbf{k}, \mathbf{r}) + c_{B,g_1(g_2)} \varphi_{Bs}(\mathbf{k}, \mathbf{r}), \quad (\text{A2})$$

where  $\varphi_{As}(\mathbf{k}, \mathbf{r})$  and  $\varphi_{Bs}(\mathbf{k}, \mathbf{r})$  are the basis set formed by the  $1s$  orbital:  $\varphi_{As}(\mathbf{k}, \mathbf{r}) = \frac{1}{\sqrt{N}} \sum_j e^{i\mathbf{k}\mathbf{R}_j^A} \phi_s(\mathbf{r} - \mathbf{R}_j^A)$ ,  $\varphi_{Bs}(\mathbf{k}, \mathbf{r}) = \frac{1}{\sqrt{N}} \sum_j e^{i\mathbf{k}\mathbf{R}_j^B} \phi_s(\mathbf{r} - \mathbf{R}_j^B)$ , in which  $\phi_s(\mathbf{r})$  is the wave function of the  $1s$  orbital in graphene.

The corresponding tight-binding Hamiltonian  $H_g$  of the core bands are  $H_g = \begin{pmatrix} \epsilon_g & \gamma_g f(\mathbf{k}) \\ \gamma_g f^*(\mathbf{k}) & \epsilon_g \end{pmatrix}$ , in which  $\epsilon_g = \langle \phi_s(\mathbf{r}) | \hat{H}_0 | \phi_s(\mathbf{r}) \rangle = -280$  eV and  $\gamma_g = \langle \phi_s(\mathbf{r}) | \hat{H}_0 | \phi_s(\mathbf{r} - \delta_i) \rangle$  approximates to be 0. The diagonalization of  $H_g$  matrix can yield energy eigenvalues  $\epsilon_{g_1}(\mathbf{k}) = \epsilon_g - \gamma_g |f(\mathbf{k})|$  and  $\epsilon_{g_2}(\mathbf{k}) = \epsilon_g + \gamma_g |f(\mathbf{k})|$ . The coefficients in the eigenvectors (A2) are obtained as  $c_{A,g_1} = c_{A,g_2} = \frac{\sqrt{2}}{2} e^{-i\varphi_{\mathbf{k}}/2}$ ,  $c_{B,g_1} = -c_{B,g_2} = -\frac{\sqrt{2}}{2} e^{i\varphi_{\mathbf{k}}/2}$ .

According to Eqs. (A1) and (A2), one can evaluate the transition dipole elements  $\mathbf{D}_{mn}(\mathbf{k}) = \langle \psi_m^{\mathbf{k}}(\mathbf{r}) | \mathbf{r} | \psi_n^{\mathbf{k}}(\mathbf{r}) \rangle$

$$\mathbf{D}_{g_1 v}(\mathbf{k}) = \mathbf{D}_{g_2 c}(\mathbf{k}) = r_z \mathbf{e}_z, \quad (\text{A3a})$$

$$\mathbf{D}_{g_1 c}(\mathbf{k}) = \mathbf{D}_{g_2 v}(\mathbf{k}) = 0, \quad (\text{A3b})$$

$$\mathbf{D}_{g_1 g_1}(\mathbf{k}) = \mathbf{D}_{g_2 g_2}(\mathbf{k}) = 0, \quad (\text{A3c})$$

$$\mathbf{D}_{g_1 g_2}(\mathbf{k}) = \mathbf{D}_{g_2 g_1}(\mathbf{k}) = 0, \quad (\text{A3d})$$

in which  $r_z = \int dz \phi_s^*(z) z \phi_p(z) = 0.041 \text{ \AA}$  [26].

Note that in our model, the transition dipole elements  $\mathbf{D}_{g_1 v}(\mathbf{k})$ ,  $\mathbf{D}_{g_2 c}(\mathbf{k})$ ,  $\mathbf{D}_{g_1 c}(\mathbf{k})$ , and  $\mathbf{D}_{g_2 v}(\mathbf{k})$  are a little bit different from those of Ref. [26]. This difference arises from that we consider the weak interaction between the nearest-neighbor  $1s$  orbitals, based on which the core-band wave functions are evaluated by Eq. (A2). In contrast, in Ref. [26], authors assume that there is no interaction between  $1s$  orbitals of two sublattices A and B, so that the wave functions of the core bands are approximated to be  $\psi_{g_1}^{\mathbf{k}}(\mathbf{r}) = \varphi_{As}(\mathbf{k}, \mathbf{r})$ ,  $\psi_{g_2}^{\mathbf{k}}(\mathbf{r}) =$

$\varphi_{Bs}(\mathbf{k}, \mathbf{r})$ . Although there exist some differences in transition dipole elements, we find the calculated ATAS are almost identical.

### APPENDIX B: ANALYTICAL DEDUCTION OF THE ATAS BASED ON THE SIMPLIFIED MODEL

We deduce the analytical results of the ATAS based on the simplified model shown in Fig. 3(e). Because the x-ray pulse is relatively short and weak, it can be approximated to a  $\delta$  function  $E_X(t) = A_X \delta(t)$ . In the simplified model, the electrons can be instantaneously excited from the  $g$  band to the  $c$  band by the x-ray pulse. According to perturbation theory and Eq. (2), the density matrix elements change from  $\rho_{gg}(\mathbf{k}_t, t < 0^-, t_d) = 1$ ,  $\rho_{cc}(\mathbf{k}_t, t < 0^-, t_d) = 0$ , and  $\rho_{cg}(\mathbf{k}_t, t < 0^-, t_d) = 0$  to  $\rho_{gg}(\mathbf{k}_t, t = 0^+, t_d) \approx 1$ ,  $\rho_{cc}(\mathbf{k}_t, t = 0^+, t_d) \approx 0$ , and  $\rho_{cg}(\mathbf{k}_t, t = 0^+, t_d) \approx -iA_X r_z$ . Next, the time-dependent evolution of density matrix elements is dominated only by IR laser, and one can obtain  $\rho_{cg}(\mathbf{k}_t, t > 0^+, t_d) = -iA_X r_z e^{-i \int_0^t (\epsilon_c(\mathbf{k} + A_I(t', t_d)) - \epsilon_g) dt'} e^{-\Gamma_0 t}$ . According to Eq. (4), when  $t < 0^-$ , the time-dependent dipole is  $\mu_{\mathbf{k}}(t, t_d) = 0$ , and

when  $t > 0^+$ , it is

$$\mu_{\mathbf{k}}(t, t_d) = -2A_X r_z^2 \sin \left[ \int_0^t \{\epsilon_c[\mathbf{k} + A_I(t', t_d)] - \epsilon_g\} dt' \right] e^{-\Gamma_0 t}. \quad (\text{B1})$$

According to Eqs. (3) and (4), the response function is calculated by  $S(\omega, t_d) = \sum_{\mathbf{k}} S_{\mathbf{k}}(\omega, t_d)$  and  $S_{\mathbf{k}}(\omega, t_d) = 2 \text{Im}[\tilde{\mu}_{\mathbf{k}}(\omega, t_d) \tilde{E}_X^*(\omega)] \propto \text{Im}[\tilde{\mu}_{\mathbf{k}}(\omega, t_d)]$ . When the IR laser is off, the time-dependent dipole is  $\mu_{\mathbf{k}}^X(t) = -2A_X r_z^2 \sin[(\epsilon_c(\mathbf{k}) - \epsilon_g)t] e^{-\Gamma_0 t}$  for  $t > 0^+$ . The response function is

$$S_{\mathbf{k}}^X(\omega) \propto \text{Im}[\tilde{\mu}_{\mathbf{k}}^X(\omega)] = \text{Im} \left[ \int_0^\infty \mu_{\mathbf{k}}^X(t) e^{-i\omega t} dt \right] \propto \frac{\Gamma_0}{\Gamma_0^2 + \{\omega - [\epsilon_c(\mathbf{k}) - \epsilon_g]\}^2}, \quad (\text{B2})$$

where we have omitted the off-resonant term of  $\frac{\Gamma_0}{\Gamma_0^2 + \{\omega + [\epsilon_c(\mathbf{k}) - \epsilon_g]\}^2}$ .

When the IR laser is turned on, the time-dependent dipole of Eq. (B1) can be deduced to be

$$\begin{aligned} \mu_{\mathbf{k}}(t, t_d) = & -2A_X r_z^2 \sin \left[ \epsilon_c(\mathbf{k})t - \epsilon_g t + \nabla_{\mathbf{k}} \epsilon_c(\mathbf{k}) \int_0^t A_I(t', t_d) dt' \right. \\ & \left. + \frac{1}{2} \nabla_{\mathbf{k}}^2 \epsilon_c(\mathbf{k}) \int_0^t A_I^2(t', t_d) dt' + \frac{1}{6} \nabla_{\mathbf{k}}^3 \epsilon_c(\mathbf{k}) \int_0^t A_I^3(t', t_d) dt' + \right] e^{-\Gamma_0 t}. \end{aligned} \quad (\text{B3})$$

For both the  $\Gamma$  and  $M$  points in the 1D two-band structure, one can obtain  $\nabla_{\mathbf{k}} \epsilon_c(\mathbf{k}) = 0$  and  $\nabla_{\mathbf{k}}^3 \epsilon_c(\mathbf{k}) = 0$ , and we ignore the higher-order terms of Eq. (B3). To simplify the integral with respect to time in Eq. (B3), we consider the vector potential  $A_I(t, t_d) = A_{I0} f_I(t + t_d) \cos(\omega_I t + \omega_I t_d) \approx A_{I0} f_I(t_d) \cos(\omega_I t + \varphi)$ , with  $\varphi = \omega_I t_d$ , and the time-dependent dipole can be approximated as

$$\begin{aligned} \mu_{\mathbf{k}}(t, t_d) & \approx -2A_X r_z^2 \sin \left[ \epsilon_c(\mathbf{k})t - \epsilon_g t + \frac{1}{2} \nabla_{\mathbf{k}}^2 \epsilon_c(\mathbf{k}) A_{I0}^2 f_I^2(t_d) \int_0^t \frac{\cos(2\omega_I t' + 2\varphi) + 1}{2} dt' \right] e^{-\Gamma_0 t} \\ & = -2A_X r_z^2 \sin[a_{\mathbf{k}}(t_d)t + b_{\mathbf{k}}(t_d) \sin(2\omega_I t + 2\varphi) + \phi(t_d)] e^{-\Gamma_0 t} \\ & = -2A_X r_z^2 \{\sin[a_{\mathbf{k}}(t_d)t + \phi(t_d)] \cos[b_{\mathbf{k}}(t_d) \sin(2\omega_I t + 2\varphi)] + \cos[a_{\mathbf{k}}(t_d)t + \phi(t_d)] \sin[b_{\mathbf{k}}(t_d) \sin(2\omega_I t + 2\varphi)]\} e^{-\Gamma_0 t}, \end{aligned} \quad (\text{B4})$$

where  $a_{\mathbf{k}}(t_d) = \epsilon_c(\mathbf{k}) - \epsilon_g + A_{I0}^2 f_I^2(t_d)/(4m_{\mathbf{k}}^*)$ ,  $b_{\mathbf{k}}(t_d) = A_{I0}^2 f_I^2(t_d)/(8\omega_I m_{\mathbf{k}}^*)$ , with effective mass  $m_{\mathbf{k}}^* = 1/\nabla_{\mathbf{k}}^2 \epsilon_c(\mathbf{k})$  for lattice momentum  $\mathbf{k}$ , and  $\phi(t_d) = -b_{\mathbf{k}}(t_d) \sin(2\varphi)$ .

Utilizing Jacobi-Anger expansion formulas, Eq. (B4) can be further deduced to be

$$\begin{aligned} \mu_{\mathbf{k}}(t, t_d) = & -2A_X r_z^2 J_0[b_{\mathbf{k}}(t_d)] \sin[a_{\mathbf{k}}(t_d)t + \phi(t_d)] e^{-\Gamma_0 t} - 2A_X r_z^2 \sum_{m=1}^{+\infty} J_{2m}[b_{\mathbf{k}}(t_d)] \sin\{[a_{\mathbf{k}}(t_d) + 4m\omega_I]t \\ & + [\phi(t_d) + 4m\varphi]\} e^{-\Gamma_0 t} - 2A_X r_z^2 \sum_{m=1}^{+\infty} J_{2m}[b_{\mathbf{k}}(t_d)] \sin\{[a_{\mathbf{k}}(t_d) - 4m\omega_I]t + [\phi(t_d) - 4m\varphi]\} e^{-\Gamma_0 t} \\ & - 2A_X r_z^2 \sum_{m=1}^{+\infty} J_{2m-1}[b_{\mathbf{k}}(t_d)] \sin\{[(4m-2)\omega_I + a_{\mathbf{k}}(t_d)]t + [(4m-2)\varphi + \phi(t_d)]\} e^{-\Gamma_0 t} \\ & - 2A_X r_z^2 \sum_{m=1}^{+\infty} J_{2m-1}[b_{\mathbf{k}}(t_d)] \sin\{[(4m-2)\omega_I - a_{\mathbf{k}}(t_d)]t + (4m-2)\varphi - \phi(t_d)\} e^{-\Gamma_0 t}, \end{aligned} \quad (\text{B5})$$

where  $J_n(x)$  is the  $n$ th-order Bessel function.

The response function is evaluated by

$$\begin{aligned}
S_{\mathbf{k}}(\omega, t_d) &\propto \text{Im}[\tilde{\mu}_{\mathbf{k}}(\omega, t_d)] = \text{Im} \left[ \int_0^\infty \mu_{\mathbf{k}}(t, t_d) e^{-i\omega t} dt \right] \\
&\propto J_0[b_{\mathbf{k}}(t_d)] \{ L[\omega, a_{\mathbf{k}}(t_d)] \cos[\phi(t_d)] + F(\omega, a_{\mathbf{k}}(t_d)) \sin[\phi(t_d)] \} \\
&\quad + \sum_{m=1}^{+\infty} J_{2m-1}[b_{\mathbf{k}}(t_d)] L[\omega, a_{\mathbf{k}}(t_d) + (4m-2)\omega_I] \cos[\phi(t_d) + (4m-2)\varphi] \\
&\quad + \sum_{m=1}^{+\infty} J_{2m-1}[b_{\mathbf{k}}(t_d)] F[\omega, a_{\mathbf{k}}(t_d) + (4m-2)\omega_I] \sin[\phi(t_d) + (4m-2)\varphi] \\
&\quad - \sum_{m=1}^{+\infty} J_{2m-1}[b_{\mathbf{k}}(t_d)] L[\omega, a_{\mathbf{k}}(t_d) - (4m-2)\omega_I] \cos[\phi(t_d) - (4m-2)\varphi] \\
&\quad - \sum_{m=1}^{+\infty} J_{2m-1}[b_{\mathbf{k}}(t_d)] F[\omega, a_{\mathbf{k}}(t_d) - (4m-2)\omega_I] \sin[\phi(t_d) - (4m-2)\varphi] \\
&\quad + \sum_{m=1}^{+\infty} J_{2m}[b_{\mathbf{k}}(t_d)] L[\omega, a_{\mathbf{k}}(t_d) + 4m\omega_I] \cos[\phi(t_d) + 4m\varphi] \\
&\quad + \sum_{m=1}^{+\infty} J_{2m}[b_{\mathbf{k}}(t_d)] F[\omega, a_{\mathbf{k}}(t_d) + 4m\omega_I] \sin[\phi(t_d) + 4m\varphi] \\
&\quad + \sum_{m=1}^{+\infty} J_{2m}[b_{\mathbf{k}}(t_d)] L[\omega, a_{\mathbf{k}}(t_d) - 4m\omega_I] \cos[\phi(t_d) - 4m\varphi] \\
&\quad + \sum_{m=1}^{+\infty} J_{2m}[b_{\mathbf{k}}(t_d)] F[\omega, a_{\mathbf{k}}(t_d) - 4m\omega_I] \sin[\phi(t_d) - 4m\varphi], \tag{B6}
\end{aligned}$$

where  $L(\omega, x) = \frac{\Gamma_0}{\Gamma_0^2 + (\omega - x)^2}$  and  $F(\omega, x) = \frac{\omega - x}{\Gamma_0^2 + (\omega - x)^2}$  are Lorentzian and Fano line shapes centered at  $x$ , respectively. In Eq. (B6), we have omitted the terms of  $L(-\omega, x)$  and  $F(-\omega, x)$  that are off-resonant, and in the last step of the derivation, the prefactors have been adjusted to be 1.

When the IR laser intensity and wavelength are  $1 \times 10^{11}$  W/cm<sup>2</sup> and 3000 nm, respectively, one can obtain  $b_{\mathbf{k}\Gamma}(t_d = 0) = A_{I0}^2 / (8\omega_I m_{\mathbf{k}\Gamma}^*) = -0.11$  and  $b_{\mathbf{k}M}(t_d = 0) = A_{I0}^2 / (8\omega_I m_{\mathbf{k}M}^*) = 0.33$ . Namely,  $|b_{\mathbf{k}}(t_d)| \leq 0.33$  for both the  $\Gamma$  and  $M$  points, and we can consider  $J_{n \geq 2}[b_{\mathbf{k}}(t_d)] \approx 0$ . In addition, because of  $|b_{\mathbf{k}}(t_d)| \leq 0.33$ , we can adopt two approximations  $\cos(\phi(t_d)) = \cos[-b_{\mathbf{k}}(t_d) \sin(2\varphi)] \approx J_0[b_{\mathbf{k}}(t_d)] \approx 1$  and  $\sin(\phi(t_d)) = \sin[-b_{\mathbf{k}}(t_d) \sin(2\varphi)] \approx 0$ .

According to Eq. (B6), the response function is reduced to

$$\begin{aligned}
S_{\mathbf{k}}(\omega, t_d) &\propto J_0[b_{\mathbf{k}}(t_d)] L[\omega, a_{\mathbf{k}}(t_d)] + J_1[b_{\mathbf{k}}(t_d)] L[\omega, a_{\mathbf{k}}(t_d) + 2\omega_I] \cos(2\omega_I t_d) + J_1[b_{\mathbf{k}}(t_d)] F[\omega, a_{\mathbf{k}}(t_d) + 2\omega_I] \sin(2\omega_I t_d) \\
&\quad - J_1[b_{\mathbf{k}}(t_d)] L[\omega, a_{\mathbf{k}}(t_d) - 2\omega_I] \cos(2\omega_I t_d) + J_1[b_{\mathbf{k}}(t_d)] F[\omega, a_{\mathbf{k}}(t_d) - 2\omega_I] \sin(2\omega_I t_d). \tag{B7}
\end{aligned}$$

The ATAS of the electron with  $\mathbf{k}$  is evaluated by

$$\Delta S_{\mathbf{k}}(\omega, t_d) = S_{\mathbf{k}}(\omega, t_d) - S_{\mathbf{k}}^X(\omega). \tag{B8}$$

- 
- [1] M. Hentschel, R. Kienberger, Ch. Spielmann, G. A. Reider, N. Milosevic, T. Brabec, P. Corkum, U. Heinzmann, M. Drescher, and F. Krausz, Attosecond metrology, *Nature (London)* **414**, 509 (2001).
- [2] F. Krausz and M. Ivanov, Attosecond physics, *Rev. Mod. Phys.* **81**, 163 (2009).
- [3] T. Gaumnitz, A. Jain, Y. Pertot, M. Huppert, I. Jordan, F. Ardana-Lamas, and H. J. Wörner, Streaking of 43-attosecond soft-X-ray pulses generated by a passively CEP-stable mid-infrared driver, *Opt. Express* **25**, 27506 (2017).
- [4] A. L. Cavalieri, N. Mueller, T. Uphues, V. S. Yakovlev, A. Baltuska, B. Horvath, B. Schmidt, L. Bluemel, R. Holzwarth, S. Hendel *et al.*, Attosecond spectroscopy in condensed matter, *Nature (London)* **449**, 1029 (2007).
- [5] E. Goulielmakis, Z.-H. Loh, A. Wirth, R. Santra, N. Rohringer, V. S. Yakovlev, S. Zherebtsov, T. Pfeifer, A. M. Azzeer, M. F. Kling *et al.*, Real-time observation of valence electron motion, *Nature (London)* **466**, 739 (2010).
- [6] M. B. Gaarde, C. Buth, J. L. Tate, and K. J. Schafer, Transient absorption and reshaping of ultrafast XUV

- light by laser-dressed helium, *Phys. Rev. A* **83**, 013419 (2011).
- [7] A. R. Beck, D. M. Neumark, and S. R. Leone, Probing ultrafast dynamics with attosecond transient absorption, *Chem. Phys. Lett.* **624**, 119 (2015).
- [8] M. Wu, S. Chen, S. Camp, K. J. Schafer, and M. B. Gaarde, Theory of strong-field attosecond transient absorption, *J. Phys. B* **49**, 062003 (2016).
- [9] H. Wang, M. Chini, S. Chen, C.-H. Zhang, F. He, Y. Cheng, Y. Wu, U. Thumm, and Z. Chang, Attosecond Time-Resolved Autoionization of Argon, *Phys. Rev. Lett.* **105**, 143002 (2010).
- [10] M. Holler, F. Schapper, L. Gallmann, and U. Keller, Attosecond Electron Wave-Packet Interference Observed by Transient Absorption, *Phys. Rev. Lett.* **106**, 123601 (2011).
- [11] Z. Q. Yang, D. F. Ye, T. Ding, T. Pfeifer, and L. B. Fu, Attosecond XUV absorption spectroscopy of doubly excited states in helium atoms dressed by a time-delayed femtosecond infrared laser, *Phys. Rev. A* **91**, 013414 (2015).
- [12] J. E. Bækhoj and L. B. Madsen, Attosecond transient-absorption spectroscopy on aligned molecules, *Phys. Rev. A* **94**, 043414 (2016).
- [13] P. M. Kraus, M. Zürich, S. K. Cushing, D. M. Neumark, and S. R. Leone, The ultrafast X-ray spectroscopic revolution in chemical dynamics, *Nat. Rev. Chem.* **2**, 82 (2018).
- [14] R. Geneaux, H. J. B. Marroux, A. Guggenmos, D. M. Neumark, and S. R. Leone, Transient absorption spectroscopy using high harmonic generation: A review of ultrafast x-ray dynamics in molecules and solids, *Philos. Trans. R. Soc. A* **377**, 20170463 (2019).
- [15] S. Chen, M. Wu, M. B. Gaarde, and K. J. Schafer, Quantum interference in attosecond transient absorption of laser-dressed helium atoms, *Phys. Rev. A* **87**, 033408 (2013).
- [16] M. Chini, B. Zhao, H. Wang, Y. Cheng, S. X. Hu, and Z. Chang, Subcycle ac Stark Shift of Helium Excited States Probed with Isolated Attosecond Pulses, *Phys. Rev. Lett.* **109**, 073601 (2012).
- [17] X. Wu, Z. Yang, S. Zhang, X. Ma, J. Liu, and D. Ye, Buildup time of Autler-Townes splitting in attosecond transient absorption spectroscopy, *Phys. Rev. A* **103**, L061102 (2021).
- [18] X. Wu, S. Zhang, and D. Ye, Clocking the buildup dynamics of light-induced states through attosecond transient absorption spectrum, *J. Phys. B* **54**, 205602 (2021).
- [19] M. Schultze, K. Ramasesha, C. D. Pemmaraju, S. A. Sato, D. Whitmore, A. Gandman, J. S. Prell, L. J. Borja, D. Prendergast, and K. Yabana, Attosecond band-gap dynamics in silicon, *Science* **346**, 1348 (2014).
- [20] M. Lucchini, S. A. Sato, A. Ludwig, J. Herrmann, M. Volkov, L. Kasmi, Y. Shinohara, K. Yabana, L. Gallmann, and U. Keller, Attosecond dynamical Franz-Keldysh effect in polycrystalline diamond, *Science* **353**, 916 (2016).
- [21] F. Schlaepfer, M. Lucchini, S. A. Sato, M. Volkov, L. Kasmi, N. Hartmann, A. Rubio, L. Gallmann, and U. Keller, Attosecond optical-field-enhanced carrier injection into the GaAs conduction band, *Nat. Phys.* **14**, 560 (2018).
- [22] M. Volkov, S. A. Sato, F. Schlaepfer, L. Kasmi, N. Hartmann, M. Lucchini, L. Gallmann, A. Rubio, and U. Keller, Attosecond screening dynamics mediated by electron localization in transition metals, *Nat. Phys.* **15**, 1145 (2019).
- [23] T. Otobe, Attosecond electro-optic effect in zinc sulfide induced by a laser field, *Phys. Rev. A* **100**, 033401 (2019).
- [24] M. Lucchini, S. A. Sato, G. D. Lucarelli, B. Moio, G. Inzani, R. Borrego-Varillas, F. Frassetto, L. Poletto, H. Hübener, U. De Giovannini *et al.*, Unravelling the intertwined atomic and bulk nature of localised excitons by attosecond spectroscopy, *Nat. Commun.* **12**, 1021 (2020).
- [25] S. A. Sato, H. Hübener, U. De Giovannini, and A. Rubio, Ab initio simulation of attosecond transient absorption spectroscopy in two-dimensional materials, *Appl. Sci.* **8**, 1777 (2018).
- [26] G. Cistaro, L. Plaja, F. Martín, and A. Picón, Attosecond x-ray transient absorption spectroscopy in graphene, *Phys. Rev. Res.* **3**, 013144 (2021).
- [27] T. Otobe, Y. Shinohara, S. A. Sato, and K. Yabana, Femtosecond time-resolved dynamical Franz-Keldysh effect, *Phys. Rev. B* **93**, 045124 (2016).
- [28] T. Otobe, Analytical formulation for modulation of time-resolved dynamical Franz-Keldysh effect by electron excitation in dielectrics, *Phys. Rev. B* **96**, 235115 (2017).
- [29] S. Yamada and K. Yabana, Symmetry properties of attosecond transient absorption spectroscopy in crystalline dielectrics, *Phys. Rev. B* **101**, 165128 (2020).
- [30] P. R. Wallace, The band theory of graphite, *Phys. Rev.* **71**, 622 (1947).
- [31] A. H. Castro Neto, F. Guinea, N. M. R. Peres, K. S. Novoselov, and A. K. Geim, The electronic properties of graphene, *Rev. Mod. Phys.* **81**, 109 (2009).
- [32] N. Yoshikawa, T. Tamaya, and K. Tanaka, High-harmonic generation in graphene enhanced by elliptically polarized light excitation, *Science* **356**, 736 (2017).
- [33] I. Alonso Calafell, L. A. Rozema, D. A. Iranzo, A. Trenti, P. K. Jenke, J. D. Cox, A. Kumar, H. Bieliaiev, S. Nanot, C. Peng *et al.*, Giant enhancement of third-harmonic generation in graphene-metal heterostructures, *Nat. Nanotechnol.* **16**, 318 (2021).
- [34] F. Dong, Q. Xia, and J. Liu, Ellipticity of the harmonic emission from graphene irradiated by a linearly polarized laser, *Phys. Rev. A* **104**, 033119 (2021).
- [35] H. K. Keldar, U. Saalman, and J. M. Rost, Ultrashort laser-driven dynamics of massless Dirac electrons generating valley polarization in graphene, *Phys. Rev. Res.* **4**, L022014 (2022).
- [36] F. Dong and J. Liu, Knee structure in the laser-intensity dependence of harmonic generation for graphene, *Phys. Rev. A* **106**, 043103 (2022).
- [37] G. Vampa, C. R. McDonald, G. Orlando, D. D. Klug, P. B. Corkum, and T. Brabec, Theoretical Analysis of High-Harmonic Generation in Solids, *Phys. Rev. Lett.* **113**, 073901 (2014).
- [38] S. C. Jiang, H. Wei, J. G. Chen, C. Yu, R. F. Lu, and C. D. Lin, Effect of transition dipole phase on high-order harmonic generation in solid materials, *Phys. Rev. A* **96**, 053850 (2017).
- [39] W. V. Houston, Acceleration of electrons in a crystal lattice, *Phys. Rev.* **57**, 184 (1940).
- [40] W. E. Lamb, R. R. Schlicher, and M. O. Scully, Matter-field interaction in atomic physics and quantum optics, *Phys. Rev. A* **36**, 2763 (1987).
- [41] M. Scully and M. Zubairy, *Quantum Optics* (Cambridge University Press, Cambridge, 1997).

- [42] M. Wu, S. Ghimire, D. A. Reis, K. J. Schafer, and M. B. Gaarde, High-harmonic generation from Bloch electrons in solids, *Phys. Rev. A* **91**, 043839 (2015).
- [43] U. Fano, Effects of configuration interaction on intensities and phase shifts, *Phys. Rev.* **124**, 1866 (1961).
- [44] C. Ott, A. Kaldun, P. Raith, K. Meyer, M. Laux, J. Evers, C. H. Keitel, C. H. Greene, and T. Pfeifer, Lorentz meets Fano in spectral line shapes: A universal phase and its laser control, *Science* **340**, 716 (2013).
- [45] For instance, our preliminary calculations show that our theory can precisely determine the tilt angle of the V-shaped structure in the GaAs experiment of the following reference: K. Uchida, T. Otobe, T. Mochizuki, C. Kim, M. Yoshita, H. Akiyama, L. N. Pfeiffer, K. W. West, K. Tanaka, and H. Hirori, Subcycle Optical Response Caused by a Terahertz Dressed State with Phase-Locked Wave Functions, *Phys. Rev. Lett.* **117**, 277402 (2016).